Temperature-amplitude spectrum for early full-field vibration-fatigue-crack identification

Martin Česnik[a], Janko Slavič[a,*]

[a] *University of Ljubljana, Faculty of Mechanical Engineering, Aškerčeva 6, 1000 Ljubljana, Slovenia*

Cite as:
Martin Česnik and Janko Slavič, "Temperature-amplitude spectrum for early full-field vibration-fatigue-crack identification," International Journal of Mechanical Sciences 286 (2025) 109829. `doi.org/10.1016/j.ijmecsci.2024.109829`.

Abstract

A dynamic structure under vibration loading within its natural frequency range can experience failure due to vibration fatigue. Understanding the causes of such failure requires pinpointing the initiation time and location of fatigue cracks, tracking their propagation, and identifying the frequency range of critical stress responses. This research introduces a novel, thermoelasticity-based method – the Temperature-Amplitude Spectrum (TAS) method – for early-stage, full-field, and non-contact crack detection that operates during uninterrupted vibration testing. This method leverages high-speed infrared imaging to analyze the specimen's temperature-amplitude spectrum, capturing comprehensive crack-related information, including initiation and propagation, in real time. Experimentally validated on both 3D-printed polymer and aluminum specimens, the TAS method accurately identified crack locations and paths without complex adjustments to the experimental setup or data processing. This new approach advances vibration-fatigue testing by enabling reliable, high-resolution crack detection and analysis while remaining computationally efficient.

*Corresponding author. Tel.: +386 14771 226.
Email address: janko.slavic@fs.uni-lj.si

Keywords:

- vibration fatigue
- crack initiation and propagation
- thermoelasticity theory
- high-speed IR imaging
- temperature-amplitude spectrum
- early full-field crack identification

---

1. Introduction

Vibration fatigue is recognized as one of the most common failure mechanisms encountered during environmental vibration testing [1–3]. Over the past decade, this field has garnered significant attention within the scientific community. As a result, vibration fatigue analysis has evolved beyond stationary Gaussian excitation and uniaxial stress conditions [4]. Current approaches now incorporate non-Gaussian [5–10], non-stationary [11–13], and multi-axis excitations [14, 15], along with their respective stress responses [16–19]. Additionally, these studies now consider nonlinear dynamic systems [20–22]. Beyond evaluation and control across a broader range of signal types [23–25], recent research has explored the influence of material properties on vibration fatigue. This includes investigations into single-crystal superalloys [26] and various 3D-printed metals [27] and polymers [28, 29], which can also exhibit frequency-dependent fatigue parameters [30].

Vibration fatigue is commonly estimated using spectral methods [31]. However, despite the accuracy of these methods, experimental vibration tests on actual structures remain necessary, as certain vibration loads can still lead to structural vibration-fatigue failure [32]. In such instances, key information for enhancing a structure's vibration resilience includes the crack initiation time, location, severity, and the critical excitation/response frequency. Since vibration testing applies a high load rate to the structure, any interruptions for damage inspection can significantly extend the testing duration [33]. Additionally, inspecting for potential cracks typically requires dismounting, inspecting, and remounting the structure, potentially altering its boundary conditions. Therefore, to maximize insights gained from vibration tests that result in fatigue failure, it is essential to employ a real-time, non-intrusive, non-contact, and full-field method for detecting damage.

Monitoring vibration fatigue can be accomplished using methods such as vibration-based approaches [34, 35], digital image correlation (DIC) [36], and thermography [37]. Starting with vibration-based methods: crack detection typically involves observing changes in modal parameters [38] by evaluating frequency-response functions. For example, Janeliukstis *et al.* [39] demonstrated the effectiveness of the modeshape-curvature square method for crack localization. Gupta and Das [40] further enhanced this approach's accuracy by applying a neural network trained with numerical models to extract error-free frequency-response data. For complex structures, the modal-strain-energy-index method has shown high localization accuracy, as numerically shown by Zhang *et al.* [41]. Bao *et al.* [42] also demonstrated precise localization using a multiple signal classification (MUSIC) algorithm with the guided-wave method, highlighting early crack detection and full-field observations. Although vibration-based methods offer reliable crack detection, localization, and near-real-time monitoring, they are somewhat limited in versatility, constraining their applicability across various products.

Conversely, the DIC method provides more flexibility and true full-field observation. Risbet *et al.* [43] showed that DIC could detect small strains under cyclic fatigue loading as early as 2010. Later, Kovarik [44] demonstrated DIC's capability in damage detection by monitoring strain fields during vibration tests using low-speed cameras with a lock-in approach. Recently, Sun *et al.* [45] employed a high-speed camera to detect damage at high load-cycle rates, as seen in vibration fatigue. Zanarini [46] used DIC to obtain full-field frequency-response functions to establish defect acceptance criteria. However, DIC has two main drawbacks. First, obtaining strain requires double spatial differentiation, which increases noise levels [47]. Second, the high computational demand for DIC, particularly at high spatial resolutions, can be a limitation. These drawbacks are typically not present in thermographic approaches.

Thermographic damage assessment using infrared (IR) imaging is a well-established [48], non-contact technique with extensive applications, often applied in combination with thermoelastic stress analysis (TSA). D'Accardi *et al.* [49] presented conductive-thermography technique for non-destructive crack detection. Additionally, Zhu *et al.* [50] and Bercelli *et al.* [51, 52] applied infrared thermography to assess fatigue crack growth in metals, exploring the effects of heat treatments and stress ratios on crack propagation and closure. Meanwhile, Ricotta and Meneghetti [53], Amjad *et al.* [54], and Middleton *et al.* [55] explored real-time, energy-based, and cost-effective thermographic monitoring systems, emphasizing practical applications for detecting fatigue in materials and large-scale structures. Thermoelastic approach is widely used for assessing the Paris' law [56], detecting damage in composite materials [57–59] and for analyzing structural damping [60–62], though it has limitations when large displacements are involved [63].

Regardless, thermographic damage assessment continues to gain research interest, especially for high-rate loading conditions. Wei *et al.* [64] introduced a vibro-thermography method that uses an IR camera to identify fatigue cracks in specimens excited by a piezoelectric transducer in the ultrasonic range. Recently, Cai *et al.* [65] developed a method for monitoring fatigue damage in steel specimens during vibration testing, using a low-speed IR camera to observe heat generated by the specimen's resonant response at approximately 200

Hz. When subjected to vibration loads, temperature changes occur at faster rates, requiring high-speed IR imaging for accurate monitoring. For instance, Capponi *et al.* [66] estimated fatigue damage in a Y-shaped specimen under random-signal multi-axial excitation, while Zaletelj *et al.* [47] applied the thermoelastic principle to identify strain modeshapes in metal beams, capturing IR data at 5000 frames per second. Recently, Šonc *et al.* [67] showed that thermoelasicity principle can also be used as a criterion for vibration fatigue under multiaxial loading.

Building on these advancements, the thermoelasticity approach presents a promising non-contact and non-invasive method for crack detection during vibration fatigue. This study addresses this potential by introducing a temperature-amplitude-spectrum (TAS) method for early crack detection using high-speed IR imaging. The TAS method is non-contact, computationally efficient, and non-intrusive, facilitating continuous, accurate, and early crack detection during vibration fatigue testing without interrupting the process.

This manuscript is structured as follows. Section 2 provides an overview of the physical principles underlying structural dynamics, vibration fatigue, and thermoelasticity. The novel TAS method for identifying vibration-fatigue cracks is introduced in Section 3. Section 4 details the experimental setup, testing procedure, and the range of specimens used. In Section 5, the results of crack identification using the TAS method are presented for aluminum and 3D-printed polymer specimens. Finally, conclusions are discussed in Section 6.

2. Theoretical background

This section initially presents the fundamental principles governing vibration fatigue in the context of kinematic (base) excitation [68]. Following this, a correlation is established between the structure's stress response and its temperature field, offering real-time insights into the structural condition as observed through infrared (IR) imaging.

2.1. Vibration fatigue of base-excited structures

Vibration fatigue arises when the frequency spectrum of the excitation aligns with the natural frequencies of the structure. If the real dynamic structure can be assumed to be linear and can be discretized to an N-degrees-of-freedom system, its governing equations of motion in the case of kinematic (base) excitation are formulated as [68]:

$$\mathbf{M}\,\ddot{\boldsymbol{z}} + \mathrm{i}\,\mathbf{D}\,\boldsymbol{z} + \mathbf{K}\,\boldsymbol{z} = -\mathbf{M}\,\boldsymbol{b}\,\ddot{y}, \tag{1}$$

where $\ddot{y}$ represents the acceleration of the base, $\boldsymbol{z}$ denotes the vector of relative displacements between the structure and the base, and $\boldsymbol{b}$ indicates the directional vector linking the structure's generalized coordinates with the direction of the base movement. $\mathbf{M}, \mathbf{D}$ and $\mathbf{K}$ are the mass, damping and stiffness matrices, respectively. In Eq. (1), hysteretic damping is assumed.

Solving the eigenvalue problem on the left-hand side of Eq. (1) yields the structure's natural frequencies, ω_r, damping ratios, η_r, and a modal matrix, $\mathbf{\Phi}$ [69]. The matrix $\mathbf{\Phi}$ consists of N mass-normalized modeshapes, $\boldsymbol{\phi}_r = [\phi_{r,1}\ \phi_{r,2}\ \cdots\ \phi_{r,N}]$. Next, a vector of mode-participation factors $\boldsymbol{\Gamma} = \mathbf{\Phi}^{\mathrm{T}}\,\mathbf{M}\,\boldsymbol{b}$ [70] is introduced. Based on the linear relationship between the displacement modeshapes $\boldsymbol{\phi}_r$, strain modeshapes ${}_{\varepsilon}\boldsymbol{\phi}_r$ and stress modeshapes ${}_{\sigma}\boldsymbol{\phi}_r$ [71, 72], the stress response at the k-th stress degree-of-freedom can be expressed as [28]:

$$\sigma_k(\omega) = \sum_{r=1}^{N} \frac{\Gamma_r\ {}_{\sigma}\phi_{r,k}}{\omega_r^2 - \omega^2 + \mathrm{i}\,\eta_r\,\omega_r^2}\,\ddot{y}(\omega) = H_{\sigma\ddot{y},k}(\omega)\,\ddot{y}(\omega). \tag{2}$$

In Eq. (2), $H_{\sigma\ddot{y},k}(\omega)$ represents the structure's transmissibility, describing the influence of the base kinematics $\ddot{y}(\omega)$ on the stress response $\sigma_k(\omega)$ within the structure. Given the known power spectral density (PSD) [73] of the excitation, $G_{\ddot{y}\ddot{y}}(\omega)$, the stress response at the k-th stress degree-of-freedom can be written as:

$$G_{\sigma\sigma,k}(\omega) = \left|H_{\sigma\ddot{y},k}(\omega)\right|^2 G_{\ddot{y}\ddot{y}}(\omega). \tag{3}$$

From the perspective of vibration fatigue, dynamic structures accumulate damage due to their dynamic stress responses. The impact of a material's fatigue characteristics is quantified using Basquin's equation, $\sigma = S_f\, N^b$ [74], where S_f denotes fatigue strength and b represents the fatigue exponent. Typically, the linear damage accumulation rule is applied, where the damage D of a single stress-load cycle is defined as $D = 1/N(\sigma)$. On a macro scale, structural failure is recognized when $D = 1$. To estimate the damage accumulation rate d in the fatigue zone of a dynamically excited structure, various frequency counting methods can be applied [31]. When a single, distinct modeshape is excited, the narrowband method provides reliable results, even with its simplicity [73]:

$$d^{\mathrm{NB}} = \frac{\left(\sqrt{2\,m_0}\right)^k}{2\,\pi\,C} \sqrt{\frac{m_2}{m_0}}\;\Gamma\left(1 + \frac{k}{2}\right), \tag{4}$$

where $k = -1/b$, $C = S_f^{-1/b}$, Γ denotes the Gamma function and m_0, m_2 are the moments of the one-sided stress-response PSD $G_{\sigma\sigma,k}(\omega)$ (Eq. (3)).

2.2. Thermoelasticity principle

The principle of thermoelasticity is founded on the interaction between a solid structure's mechanical and thermodynamic responses. This principle applies the fundamental laws of continuum mechanics alongside the first and second laws of thermodynamics. Assuming a fully reversible adiabatic process, the governing equation of thermoelasticity, which relates the stress field to the temperature field, is expressed as follows [75, 76]:

$$\rho\, C_\sigma\, \frac{\dot{T}}{T} = -\left[\alpha + \left(\frac{\nu}{E^2}\,\frac{\partial E}{\partial T} - \frac{1}{E}\,\frac{\partial \nu}{\partial T}\right)\, s\right]\, \dot{s} + \left(\frac{(1+\nu)}{E^2}\,\frac{\partial E}{\partial T} - \frac{1}{E}\,\frac{\partial \nu}{\partial T}\right) \boldsymbol{\sigma}_p\, \dot{\boldsymbol{\sigma}}_p, \tag{5}$$

where ρ denotes the density, C_σ is the specific heat at constant stress, and T is the absolute temperature. Additionally, α denotes the coefficient of linear expansion, E is Young's modulus, ν is Poisson's ratio, $\boldsymbol{\sigma}_p$ is the principal stress tensor, and s is the first stress invariant.

In a uniaxial stress field, where $s = \sigma_1$ and $\sigma_2 = \sigma_3 = 0$, Eq. (5) simplifies to:

$$\rho\, C_\sigma \frac{\dot{T}}{T} = -\left(\alpha - \frac{1}{E^2}\frac{\partial E}{\partial T}\sigma_1\right)\dot{\sigma}_1. \tag{6}$$

If the principal stress load is sinusoidal, expressed as $\sigma_1(t) = \sigma_{1,\mathrm{m}} + \sigma_{1,\mathrm{a}} \sin(\omega\, t)$, the linearized solution of Eq. (6) about the reference temperature T_0 becomes [77]:

$$\frac{\rho C_\sigma}{T_0}\,\Delta T(t) = -\left(\alpha + \frac{1}{E^2}\frac{\partial E}{\partial T}\sigma_{1,\mathrm{m}}\right)\sigma_{1,\mathrm{a}} \sin(\omega\, t) + \frac{1}{4E^2}\frac{\partial E}{\partial T}\,\sigma_{1,\mathrm{a}}^2\,\cos(2\omega t). \tag{7}$$

Under the assumption of an adiabatic process, the temperature within the observed control volume – subjected to harmonic stress excitation – oscillates with both the fundamental excitation frequency ω and its second harmonic $2\,\omega$. For high-cycle fatigue conditions, resulting from the structure's dynamic response, the observed temperature range T remains narrow. In this scenario, variations in Young's modulus with respect to temperature $\partial E/\partial T$ are negligible. Consequently, Eq. (7) simplifies to:

$$\Delta T(t) = -\frac{\alpha\, T_0}{\rho\, C_\sigma}\,\sigma_{1,\mathrm{a}}\,\sin(\omega\, t) = K_m\,\sigma_{1,\mathrm{a}}\,\sin(\omega\, t), \tag{8}$$

where $K_m = -(\alpha\, T_0)/(\rho\, C_\sigma)$ is the thermoelastic coefficient [75]. The relationship between stress response and temperature at the observed location can be generalized as $\Delta T(t) = K_m \sigma(t)$ when the dynamic structure is excited in a single, well-separated mode shape, due to the narrow-band nature of the stress response (Eq. (2)).

In applying the thermoelasticity principle to the identification and quantification of fatigue cracks, the adiabatic condition can be assumed to hold across the entire observed (visible) surface, provided the observation times are sufficiently short.

As a fatigue crack develops and penetrates the material, the stresses on the observed surface near the crack are reduced, leading to an absence of temperature variations due to the thermoelastic effect , see Fig. 1. However, temperature fluctuations still occur at the crack tip. At this stage, the temperature distribution near the crack is governed by the heat-diffusion equation:

$$\frac{\partial T}{\partial t} = \frac{k}{\rho\, C_\sigma} \left(\frac{\partial^2 T}{\partial x^2} + \frac{\partial^2 T}{\partial y^2} + \frac{\partial^2 T}{\partial z^2} \right), \tag{9}$$

where k is the thermal conductivity.

3. Temperature-amplitude-spectrum (TAS) method

This section introduces the TAS method for early, full-field crack identification in structures experiencing vibration fatigue. This approach relies on capturing the complete temperature field across the surface within the fatigue zone, using a sampling frequency that significantly exceeds the structure's natural frequency.

The main concept of this methodology is illustrated in Fig. 1 and described as follows. According to Eq. (3), when a dynamic structure is excited by a random wide-band signal, it exhibits amplified stress-response amplitudes at its natural frequencies (see Fig. 1, left). Based on thermoelasticity theory (Eq. (8)), the temperature response on the structure's surface mirrors the stress response, scaled by a thermoelastic constant. Consequently, a specific natural frequency and its associated stress modeshape can be isolated within the fatigue zone.

During broad-band excitation, the stress response near a natural frequency appears as a narrowband signal [73]. The TAS method, which employs an infrared (IR) camera, provides a full-field approach that captures spatial information across the surface. As shown in Fig. 1, the stress near the crack diminishes, as maximum stress propagates with the crack tip into the structure. This reduction is also evident in the lowered maximum value of the temperature-amplitude spectrum, obtained through a fast Fourier transform [78]. The concept is further illustrated in Fig. 1.

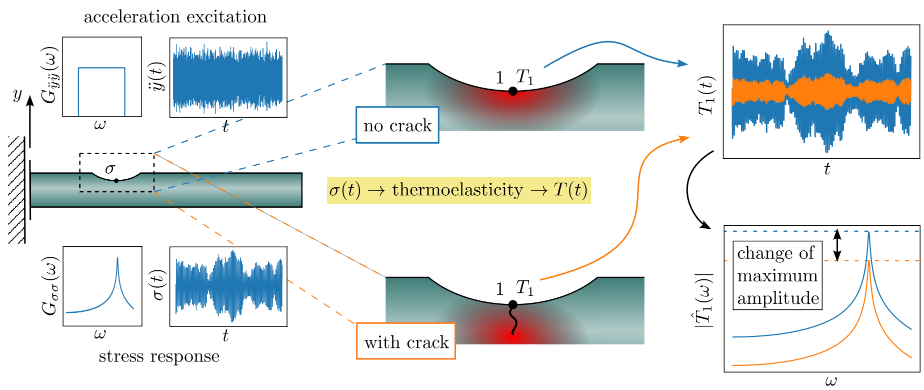

Figure 1: Crack detection concept: the temperature signal during the vibration test due to the thermoelastic effect and its changes in the presence of a crack.

In the following, the concept described above is generalized. Consider a measured temperature time series for the i-th pixel, represented as $T_i(t_n) = T_i(n \cdot \Delta t)$, where $n = 0, \ldots, N-1$. Here, Δt denotes the time step between sequential frames, and N is the total length of the time series T_i, *i. e.* the number of frames in the observed recording. Given the temperature time series $T_i(t_n)$ for the i-th pixel, the temperature-amplitude spectrum $\hat{T}_i(\omega)$ can be obtained using a discrete Fourier transform [73], expressed as $\hat{T}_i(\omega_k) = |DFT(T_i(t_n))|$, where $\omega_k = k \cdot \Delta\omega$, $k = 0, \ldots, N-1$, and $\Delta\omega = 2\pi/(N\Delta t)$. The temperature-amplitude spectrum (TAS) for the i-th pixel is defined as:

$$\hat{T}_{i,\,\mathrm{AS}} = \max(\hat{T}_i(\omega_k)), \text{ where } \omega_k \in (\omega_{\min}, \omega_{\max}), \tag{10}$$

where $\omega_{\min}$ and $\omega_{\max}$ denote the frequency range of excitation PSD $G_{\ddot{y}\ddot{y}}(\omega)$. Two conditions must be satisfied for accurate analysis. First, the structure's critical natural frequency ω_r should fall within the excitation frequency range $(\omega_{\min}, \omega_{\max})$. Second, the sampling frequency $f_s = 1/\Delta t$ must be high enough to ensure the Nyquist frequency $f_s/2$ exceeds $\omega_{\max}/2\pi$. It is important to note that the frequency of maximum magnitude may vary across different pixels; however, these peak frequencies are generally expected to cluster around the structure's critical natural frequency. The definition of the estimator $\hat{T}_{i,\,\mathrm{AS}}$ in Eq. (10) highlights the computational efficiency of the TAS method. Despite its simplicity, this method provides robust crack detection capabilities, as demonstrated in the experimental results in Sec. 5).

To compare the TAS method with the conventional thermography approach, which employs low-frame-rate infrared (IR) imaging, this study introduces an alternative image-processing technique. Due to the long exposure times associated with low-frame-rate imaging [65, 66], the temperature time series of the i-th pixel is compressed into an average temperature estimator:

$$T_{i,\mathrm{TG}} = \frac{1}{N}\sum_{n=1}^{N} T_i(t_n). \tag{11}$$

In this study, this approach is referred to as the "Thermography method".

4. Experimental research

The experimental framework developed to demonstrate the feasibility of the TAS method is outlined as follows. First, the design of the test specimens and the configuration of the experimental setup are described in detail. This is followed by a discussion of the variations among the tested specimens. Finally, preliminary experimental results are presented to provide an initial assessment of the effectiveness of the TAS method.

4.1. Experimental setup

The experimental setup follows a standard approach for vibration testing using an electrodynamic shaker, with the addition of a high-speed IR camera for enhanced measurement capabilities, as illustrated in Fig. 3a). The design of the specimens, adapted from [28] and detailed in Fig. 2(a) consists of a fixation areas, a notch area and an inertial mass. With a proposed simple design it is possible to achieve well-separated mode shape, a tuneable natural frequency, and an accessible fatigue zone (Fig. 2(b)) with a near-uniaxial stress field. To confirm the applicability of TAS methodology, the specimens were produced from PLA by 3D printing and from aluminum by conventional machining. The specimens were mounted to the shaker's armature with an M6 bolt and a 3-mm-thick aluminum plate. Additionally, to allow free movement of the specimen, the lower fixation surface was shimmed with a 3-mm aluminum plate, as depicted in Fig. 3b). For conducting vibration-fatigue tests the base excitation is defined by an acceleration random-signal PSD profile $G_{\ddot{y}\ddot{y}(\omega)}$, Eq. (3). An LDS V555 electrodynamic shaker was used, and the PSD acceleration profiles were flat-shaped (Fig. 1) with adjustable amplitude and frequency ranges. To monitor the specimen's response, a response accelerometer was employed, as shown in Fig. 3b).

For high-speed infrared (IR) imaging, a Telops FAST m3K camera was used. The camera has a specified Noise Equivalent Temperature Difference (NETD) of 32 mK; however, as demonstrated by Zaletelj *et. al* [47], significantly lower noise levels can be achieved through optimized signal processing in the frequency domain. The IR camera was fitted with a Telops 1X microscopic lens with a fixed focal distance of 26 cm. The experimental setup and its implementation are shown in Fig. 3.

4.2. Specimen overview and testing conditions

Two types of specimens were evaluated: the 3D-printed polylactic-acid (PLA) specimens and aluminum specimens. The 3D-printed PLA specimens were produced in two orientations (x and y, see Fig. 2) with an inertial mass length of $L = 24$ mm. These specimens were fabricated using a Prusa i3 MK3S+ 3D printer with a 0.4-mm nozzle diameter, a nozzle temperature of 215°C, and

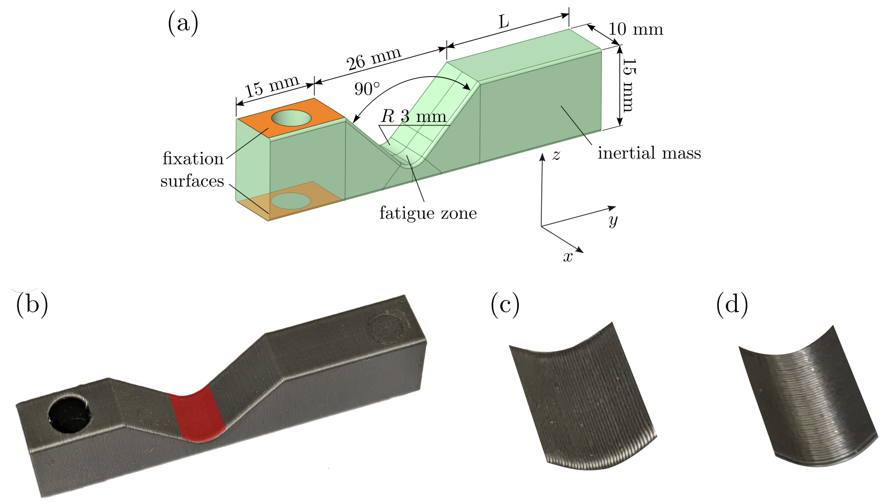

Figure 2: Specimen design; (a) specimen geometry with adopted coordinate system, (b) manufacutured specimen with denoted observed fatigue zone, (c) zoomed-in fatigue zone for specimen 3D-printed in y direction and (d) in x direction.

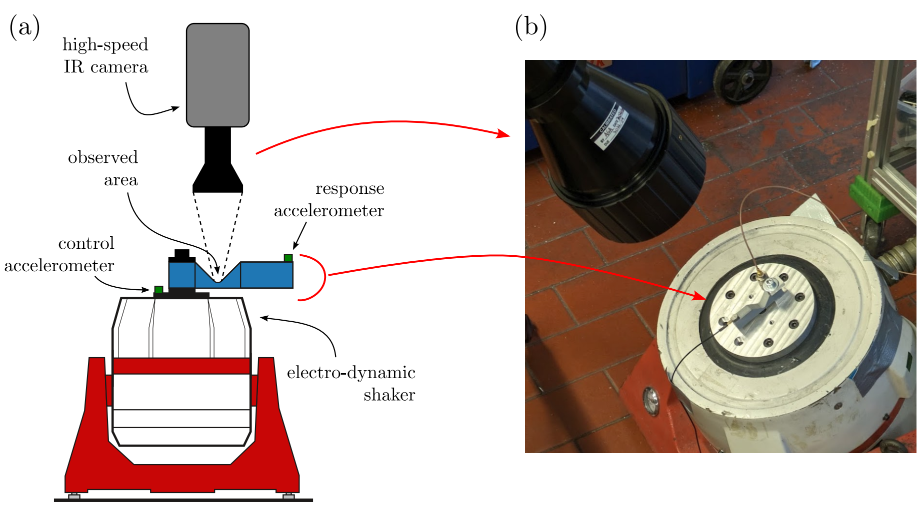

Figure 3: Experimental setup; (a) a schematic representation with an electrodynamic shaker, mounted specimen and a high-speed IR camera, (b) an actual setup.

No.	Material	L [mm]	Print direction	Surface preparation
1	PLA	24	y	/
2	PLA	24	x	/
3	Aluminum	40	/	Fine ground, black color spray coating
4	Aluminum	40	/	/

Table 1: Overview of the tested specimens.

varying printing speeds: 25 mm/s for the external perimeter, 45 mm/s for the internal perimeter, and 80 mm/s for infill. No additional surface preparation was applied to the 3D-printed specimens. Fig. 2(b) a 3D-printed specimen with a denoted area of observation during vibration testing; an enlarged view of the observed area is given in Figs. 2(c) and 2(d) for 3D printing in y and in x direction, respectively. The aluminum specimens were manufactured from 6026 aluminum alloy using water-jet cutting, with an inertial mass length of $L = 40$ mm. These specimens underwent additional surface post-processing, including fine grinding and painting with black spray to enhance IR imaging contrast. A summary of the specimen types and specifications is provided in Tab. 1.

To determine the PSD acceleration profile parameters for each test specimen, two main guidelines were followed: first, the natural frequency of the specimen needed to be continuously excited throughout the test; second, complete fatigue failure was expected to occur within 10 to 30 minutes from the start of the vibration test. The first natural frequencies of the undamaged specimens, along with the specific testing conditions for each, are provided in Tab. 2.

The high-speed camera captured IR images at a rate of 2400 frames per second, with a spatial resolution of 320×265 pixels, covering a surface area of 10.0×8.3 mm^2. IR imaging was automatically triggered at constant time intervals, capturing 1200 frames per trigger, resulting in a recorded duration of

No.	f_1 [Hz]	Excited freq. range [Hz]	PSD level [(m/s^2)^2/Hz]
1	226	[150, 400]	0.4
2	248	[150, 350]	2.0
3	505	[450, 550]	5.4
4	530	[450, 550]	4.0

Table 2: Specimens' natural frequencies and testing conditions.

0.5 seconds per interval. The control and response accelerometers sampled data at a frequency of 25.6 kHz, with a 10-second averaging period applied to obtain the specimen's frequency-response function.

4.3. Experimental results and IR image processing

According to thermoelasticity theory (Sec. 2), the temperature response of the specimen in the fatigue zone is primarily governed by the stress-response frequency. For the tested specimens, and as indicated in Eqs. (2) and (3), this frequency corresponds to the specimen's first natural frequency. The temperature response of specimen no. 1, both in the time and frequency domains, is shown in Figs. 4(a) and 4(b) after 100 seconds of vibration testing. The measured temperature data refer to pixel no. 45267, marked in Fig. 4(c) as the pixel with the highest $T_{i,\mathrm{TG}}$ value within the 0.5-second recording interval. The preliminary measurement of specimen no. 1's natural frequency (Tab. 1) demonstrates that the observed temperature response, specifically the temperature-amplitude spectrum displayed in Fig. 4(b), aligns with the analytically predicted response outlined in Eq. (8). Furthermore, the temperature-amplitude spectrum in Fig. 4(b) shows no peak at the second harmonic of the specimen's natural frequency, $2 \cdot f_1$. This observation supports the assumption of $\partial E/\partial T = 0$ in Eq. (7).

The temperature-amplitude spectrum in Fig. 4(b) shows noise within the frequency range of the highest magnitudes. To address this, Welch's averaging was applied to the temperature signals, following the method outlined in [66], which enhances the signal-to-noise ratio in the frequency domain [79]. While this approach improved the noise profile, it did not significantly enhance the accuracy of crack identification. Therefore, to reduce the computational cost associated with the TAS method, a non-averaged amplitude spectrum approach was ultimately adopted.

By calculating the TAS values as in Eq. (10) or 'Thermography' mean values as in Eq. (11), a single representative value per pixel can be obtained for each recording. These pixel values can then be visualized as a heat map, providing a graphical representation of the entire recording. Figs. 4(c) and 4(d) show the heatmaps of specimen no. 1 after 100 seconds of vibration testing, comparing the TAS method with the Thermography method. The TAS method clearly offers a more detailed visualization of the specimen's surface. In generating Fig. 4(d) the amplitude spectra values were extracted around a frequency of 225 Hz.

A response accelerometer was attached to the inertial mass of each specimen to monitor its frequency-response function during vibration-fatigue testing. By applying the least-squares complex-frequency-domain (LSCF) method [80] to the measured frequency-response data, precise information on changes (i.e., decreases) in the specimen's natural frequency and damping over the course of the vibration test was obtained. Consequently, the TAS method should also capture these shifts in the specimen's natural frequency. This prediction was validated in the present study, as illustrated in Fig. 5, where the mean frequency of the pixels' $\hat{T}_{i,\mathrm{AS}}$ values is shown alongside the natural frequency values derived from the response accelerometer. Fig. 5 further indicates that aluminum specimens exhibit a lower scatter in the averaged frequency of maximal response compared to polymer specimens. This reduced scatter may be partially due to the higher

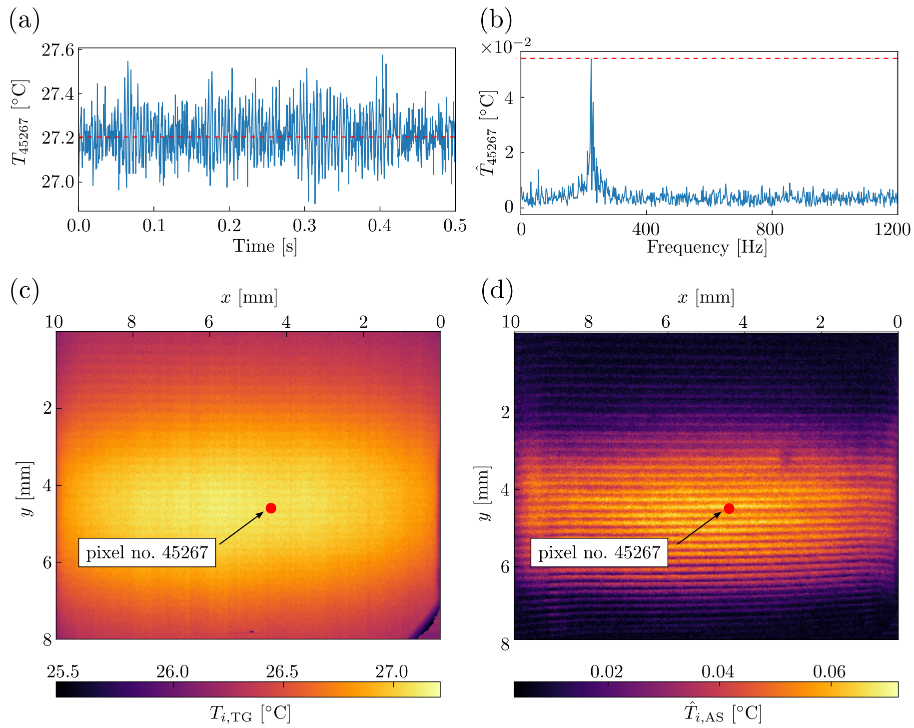

Figure 4: Temperature response of the specimen no. 1; (a) time waveform for pixel no. 45267, (b) amplitude spectrum for pixel no. 45267, (c) heatmap of observed area obtained with Thermography method and (d) with TAS method.

natural frequency of the aluminum specimens, which leads to a greater number of load cycles within each 0.5-second observation interval, enhancing the stationarity of the temperature signal. Conversely, the temperature signal of the polymer specimens shows more non-stationarity within a single 0.5-second recording, which can also be observed in the time-domain signal presented in Fig. 4.

5. Crack identification using the TAS method

The primary objective of the novel TAS method is to identify the spatial location of vibration-fatigue cracks at an early stage. Results from four tested

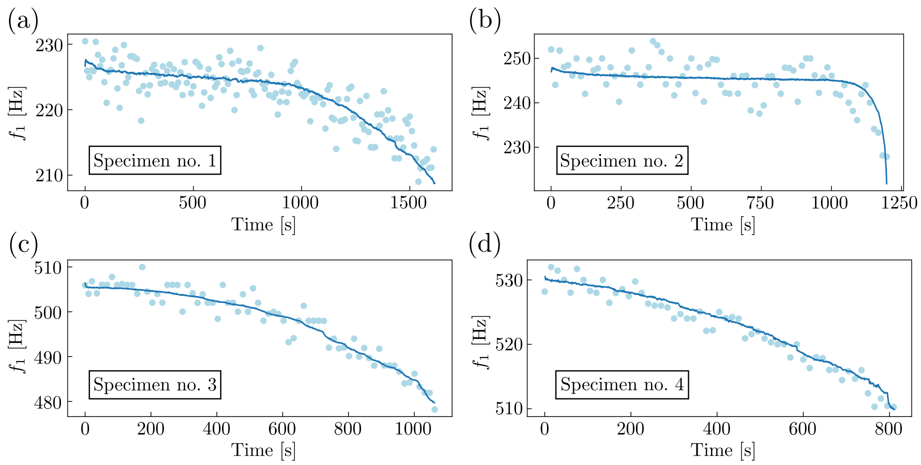

Figure 5: Comparison between (—) specimens' identified natural frequencies with a response accelerometer and (•) averaged frequency of $\hat{T}_{i,\mathrm{AS}}$, graphs (a) - (d) refer to specimens no. 1 - no. 4, respectively.

specimens, listed in Tab. 1, are presented in Figs. 6 through 9. Each figure shows a decrease in the specimen's natural frequency alongside a photograph of the resulting cracks, with jet color-mapping applied in the crack area to enhance the crack's visibility. IR images processed with the TAS method are displayed above the frequency plots, while the Thermography method results are shown below. The testing times highlighted in Figures 6-9 were chosen based on crack changes detected by the TAS method.

Examining the results for the 3D-printed specimens no. 1 and no. 2 (Figs. 6 and 7, respectively), it is clear that the TAS method offers significantly improved crack localization compared to the conventional Thermography method. As expected (Sec. 3), cracks appear as areas of locally reduced temperature in the TAS images, consistent with thermoelasticity theory (Eq. 7). As the crack propagates, these zones of reduced thermoelasticity-induced temperature expand accordingly. The final TAS image of specimen no. 1 (Fig. 6 at 1600 s), obtained with the TAS method, aligns well with the actual final crack condition.

By contrast, the Thermography method provides less detailed results, primarily identifying only the crack tips. This limitation in the Thermography method's detection efficacy arises due to heat conduction from the internal stress concentration at the crack tip to the specimen's surface, as governed by the heat diffusion law (Eq. (9)). It should also be noted that a minor printing defect was present at $x = 3$ mm and $y = 3.5$ mm in the observed area, which could have falsely suggested an early crack at 60 seconds of testing.

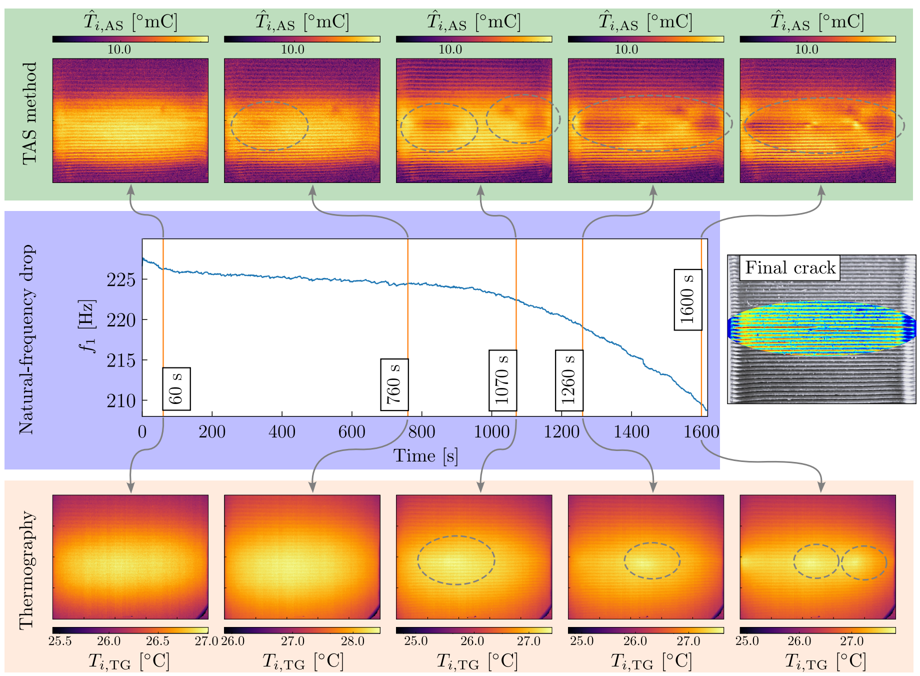

Figure 6: Crack identification of specimen no. 1 (3D printed in y direction) during vibration-fatigue testing using the TAS method (upper section) and Thermography method (bottom section) in reference to the drop of the specimen's natural frequency and a final crack in the middle section.

The results for specimen no. 2 are presented in Fig. 7. The TAS method reliably detects the failure of two individual threads, each 0.2 mm wide, appearing after 945 seconds of vibration testing. This failure is minor enough that it does not result in any detectable change in the specimen's natural frequency. As the vibration test continues, the TAS method clearly maps the propagation path of all three initial cracks. In contrast, as with specimen no. 1, the Thermography method provides significantly less detailed information on crack initiation and propagation for specimen no. 2.

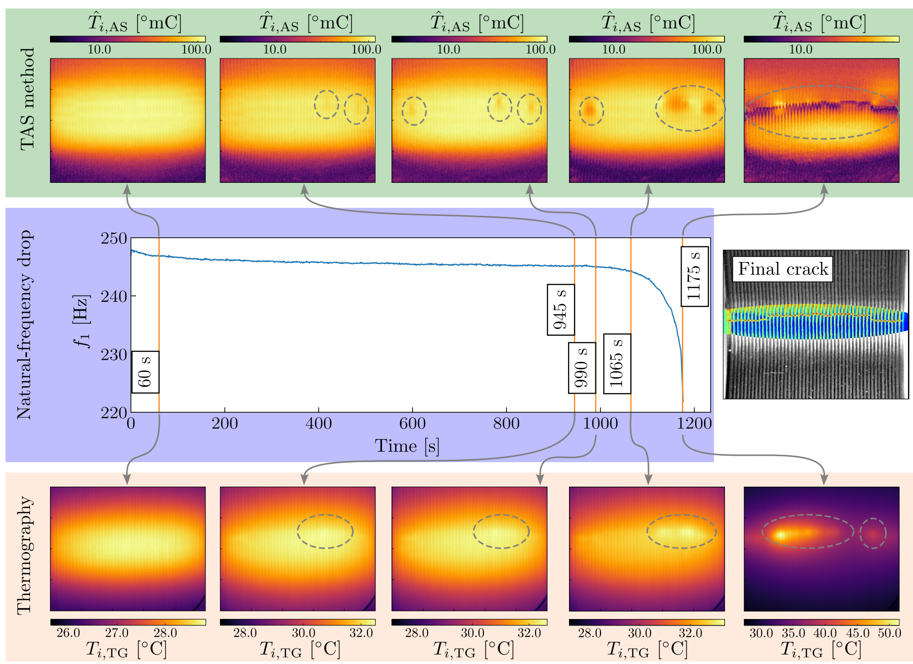

Figure 7: Crack identification of specimen no. 2 (3D printed in x direction) during vibration-fatigue testing using the TAS method (upper section) and Thermography method (bottom section) in reference to the drop of the specimen's natural frequency and a final crack in the middle section.

Additionally, the study included tests on 3D-printed specimens oriented in the z-direction (Fig. 2(a)), following the same experimental procedure. Crack detection using the TAS method on these specimens was less distinct than for those printed in the x- and y-directions, though it still yielded more accurate results than the Thermography method. The reduced effectiveness in identifying cracks is likely due to the obscured view of the crack initiation and propagation path, which is concealed beneath subsequent filament layers (for further details, see [28]).

The initial analysis of the aluminum specimens shown in Figs. 8 and 9 reveals a similar decrease in natural frequency for both specimens. In general, the TAS method reliably detects the vibration-induced fatigue crack in both cases. A closer examination of the natural frequency drop indicates that crack initiation is recognized earlier on specimen no. 3 (fine ground with black coating) than on specimen no. 4 (water-jet cut with no coating). However, the spatial accuracy of crack identification is higher for specimen no. 4 compared to no. 3. In addition to specimens no. 3 and no.4, an additional type of aluminum specimen was tested with a fine ground surface and no color coating. Crack detection on this uncoated specimen was unsuccessful due to high surface reflectivity, which led to incorrect measurements from the high-speed IR camera. Therefore, black color spraying is recommended for crack detection on reflective surfaces, although a slight increase in spatial uncertainty may be expected. It should also be noted that uneven paint application can vary paint thickness, causing random spots in the processed IR images (see Fig. 8). This issue can be effectively mitigated by comparing image changes relative to the initial test image. In contrast, the Thermography method failed to detect any cracks in the aluminum specimens. This limitation is likely due to the low heat generation and high thermal conductivity of aluminum.

Furthermore, the final crack condition in both specimens consists of multiple parallel cracks. While the TAS method reliably identifies the presence of these cracks, the accuracy in localizing the exact crack paths is reduced in such cases. This outcome aligns with expectations from thermoelastic theory, which primarily detects areas of reduced stress amplitude – areas that are often found between parallel cracks.

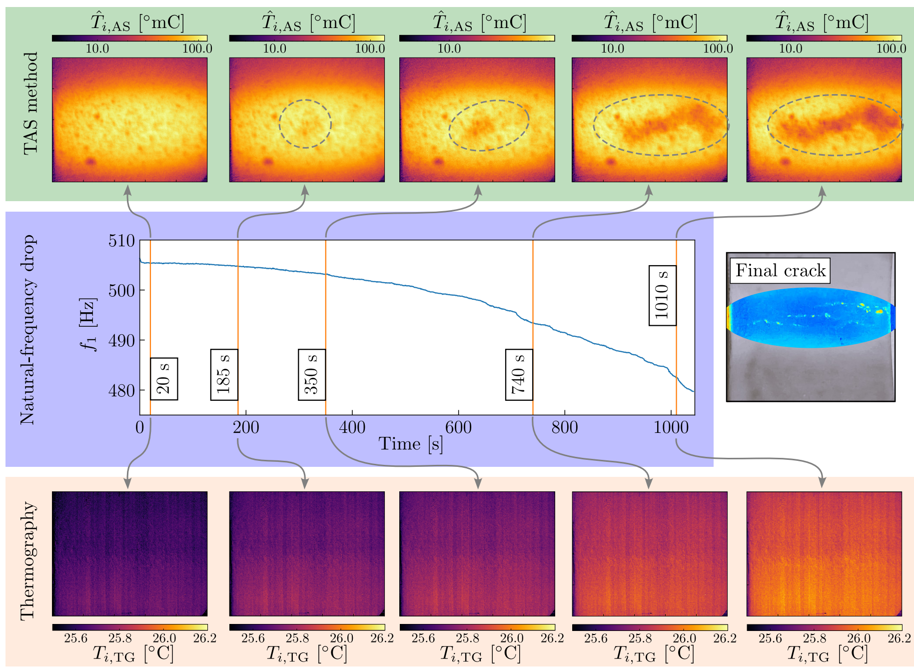

Figure 8: Crack identification of specimen no. 3 (aluminum with prepared surface) during vibration-fatigue testing using the TAS method (upper section) and Thermography method (bottom section) in reference to the drop of the specimen's natural frequency and a final crack in the middle section.

It is noteworthy that successful crack detection results were achieved with the novel TAS method on both polymer and aluminum specimens using the same image processing procedure, without any fine-tuning of the TAS method. Additionally, with a larger group of test specimens, the reliability of crack detection was consistently confirmed. In each case, a clear overview of the crack location was achieved, provided that the reflective effect was sufficiently minimized.

6. Conclusions

This study introduces a novel approach for identifying cracks due to vibration fatigue, utilizing the temperature-amplitude spectrum (TAS). The TAS method, based on thermoelastic theory and applied through high-speed IR imag-

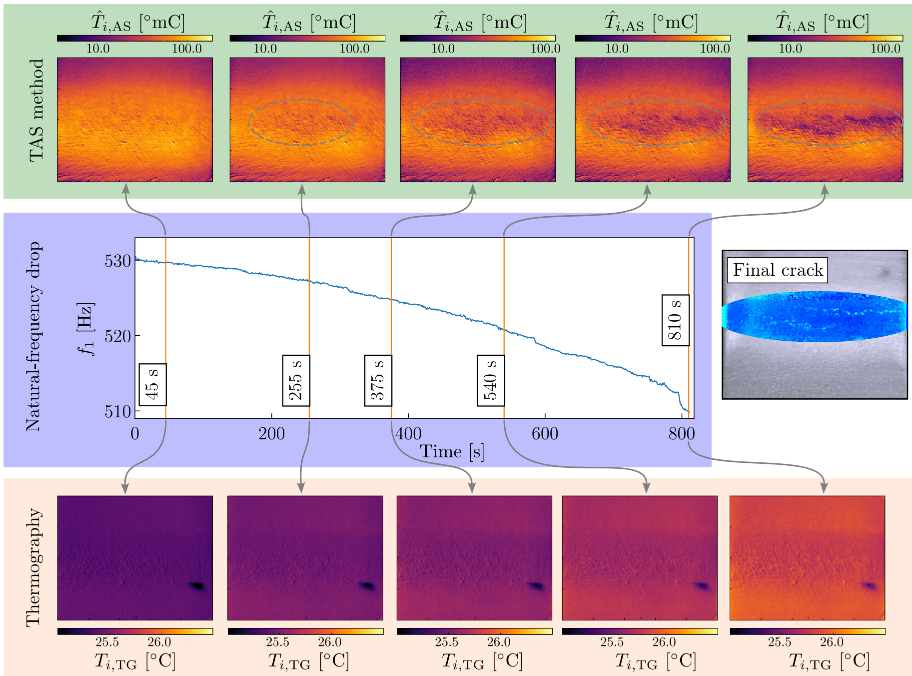

Figure 9: Crack identification of specimen no. 4 (aluminum with surface from water-jet cutting) during vibration-fatigue testing using the TAS method (upper section) and Thermography method (bottom section) in reference to the drop of the specimen's natural frequency and a final crack in the middle section.

ing, enables the real-time detection of crack initiation and progression within the specimen's fatigue zone without disrupting ongoing vibration tests. The method's effectiveness was demonstrated across multiple specimens with natural frequencies around 210 Hz and 510 Hz, highlighting its versatility in varying frequency conditions.

The established TAS method provides several distinct advantages. As a full-field, non-contact approach, it achieves high spatial resolution (320x256 pixels) and can detect early-stage cracks as small as 0.2 mm, even before any shift in natural frequency occurs. This capability allows for precise crack localization and provides detailed insights into both crack propagation and the critical frequency ranges involved in excitation and response, which are essential for assessing structural integrity under dynamic loading.

In terms of practical application, the TAS method proves as very adaptable. It performs reliably on both polymer and metal specimens without requiring adjustments of image processing procedures. The setup demands only a single measurement device, with minimal specimen surface preparation, making the method accessible for routine use. Additionally, its computational efficiency supports real-time monitoring during vibration-fatigue testing, which is crucial for early intervention and structural health monitoring.

Nevertheless, the TAS method has two primary limitations. First, reflective surfaces require a black coating to reduce interference in IR imaging. Second, the method's accuracy depends on maintaining an unobstructed view of the crack to capture clear temperature changes associated with crack initiation and propagation. Despite these limitations, the TAS method represents a significant advancement in non-destructive testing for vibration-fatigue assessment, combining practical ease with high sensitivity to early-stage damage.

Declaration of competing interest

The authors declare that they have no known competing financial interests or personal relationships that could influence the work reported in this paper.

Data availability

Data will be made available on request.

Acknowledgments

The authors acknowledge the partial financial support from the Slovenian Research Agency (research core funding no. P2-0263).

References

[1] J. Slavič, M. Mršnik, M. Česnik, J. Javh, M. Boltežar, Vibration Fatigue by Spectral Methods, 1st Edition, Elsevier, 2020.

[2] US Department of the Air Force, Military standard environmental test methods for aerospace and ground equipement, MIL-STD-810H, Method 514.8: Vibration (2019).

[3] C. Lalanne, Mechanical Vibration and Shock Analysis, Specification Development, Mechanical Vibration and Shock Analysis, Wiley, 2014.

[4] M. Česnik, J. Slavič, M. Boltežar, Uninterrupted and accelerated vibrational fatigue testing with simultaneous monitoring of the natural frequency and damping, Journal of Sound and Vibration 331 (24) (2012) 5370–5382. doi:https://doi.org/10.1016/j.jsv.2012.06.022.

[5] F. Kihm, Fatigue Life for non-Gaussian Random Excitations, Ph.D. thesis, University of Southampton (2017).

[6] M. Palmieri, M. Česnik, J. Slavič, F. Cianetti, M. Boltežar, Non-Gaussianity and non-stationarity in vibration fatigue, International Journal of Fatigue 97 (2017) 9–19. doi:https://doi.org/10.1016/j.ijfatigue.2016.12.017.

[7] J. M. E. Marques, D. Benasciutti, Variance of the fatigue damage in non-Gaussian stochastic processes with narrow-band power spectrum, Structural Safety 93 (2021) 102131. doi:https://doi.org/10.1016/j.strusafe.2021.102131.

[8] S. Cui, J. Li, S. Chen, Z. Guo, Special mathematical transformation-based fatigue damage estimation under narrowband non-gaussian random loadings, Probabilistic Engineering Mechanics 74 (2023) 103536. doi:https://doi.org/10.1016/j.probengmech.2023.103536.

[9] K. Yuan, S. Peng, Z. Sun, An artificial neural network model for fatigue damage analysis of wide-band non-gaussian random processes, Applied Ocean Research 144 (2024) 103896. doi:https://doi.org/10.1016/j.apor.2024.103896.

[10] M. Sgamma, M. Palmieri, M. Barsanti, F. Bucchi, F. Cianetti, F. Frendo, Study of the response of a single-dof dynamic system under stationary non-Gaussian random loads aimed at fatigue life assessment, Heliyon 10 (10) (2024) e30832. doi:https://10.1016/j.heliyon.2024.e30832.

[11] L. Capponi, M. Česnik, J. Slavič, F. Cianetti, M. Boltežar, Non-stationarity index in vibration fatigue: Theoretical and experimental research, International Journal of Fatigue 104 (2017) 221–230. doi:https://doi.org/10.1016/j.ijfatigue.2017.07.020.

[12] A. Trapp, P. Wolfsteiner, Fatigue assessment of non-stationary random loading in the frequency domain by a quasi-stationary Gaussian approximation, International Journal of Fatigue 148 (2021) 106214. doi:https://doi.org/10.1016/j.ijfatigue.2021.106214.

[13] A. Trapp, D. Fräulin, M. Hinz, P. Wolfsteiner, Data-driven spectral damage estimator for non-stationary vibration loading, Procedia Structural

Integrity 54 (2024) 521–535. doi:https://doi.org/10.1016/j.prostr.2024.01.115.

[14] M. Aimé, A. Banvillet, L. Khalij, E. Pagnacco, E. Chatelet, R. Dufour, A framework proposal for new multiaxial fatigue damage and extreme response spectra in random vibrations frequency analysis, Mechanical Systems and Signal Processing 213 (2024) 111338. doi:https://doi.org/10.1016/j.ymssp.2024.111338.

[15] E. Proner, E. Mucchi, R. Tovo, A relationship between fatigue damage estimation under multi-axis and single-axis random vibration, Mechanical Systems and Signal Processing 215 (2024) 111402. doi:https://doi.org/10.1016/j.ymssp.2024.111402.

[16] D. Benasciutti, D. Zanellati, A. Cristofori, The "Projection-by-Projection" (PbP) criterion for multiaxial random fatigue loadings: Guidelines to practical implementation, Frattura Ed Integrità Strutturale 13 (47) (2018) 348–366. doi:https://doi.org/10.3221/IGF-ESIS.47.26.

[17] A. T. Schmidt, N. Pandiya, Extension of the static equivalent stress hypotheses to linearly vibrating systems using wave interference – The LiWi approach, International Journal of Fatigue 147 (2021) 106103. doi:https://doi.org/10.1016/j.ijfatigue.2020.106103.

[18] A. T. Schmidt, J. Kraft, A new equivalent stress approach based on complex invariants: The coin liwi method, International Journal of Fatigue 168 (2023) 107474. doi:https://doi.org/10.1016/j.ijfatigue.2022.107474.

[19] X. Pei, Y. Cao, T. Gu, M. Xie, P. Dong, Z. Wei, J. Mei, T. Zhang, Generalizing multiaxial vibration fatigue criteria in the frequency domain: A data-driven approach, International Journal of Fatigue 186 (2024) 108390. doi:https://doi.org/10.1016/j.ijfatigue.2024.108390.

[20] E. Czerlunczakiewicz, M. Majerczak, M. Bonato, Fatigue simulations for automotive components undergoing vibration loadings: Effect of nonlinear behavior, Procedia Structural Integrity 57 (2024) 743–753. doi:https://doi.org/10.1016/j.prostr.2024.03.080.

[21] P. V. Avvari, Y. Yang, C. K. Soh, Long-term fatigue behavior of a cantilever piezoelectric energy harvester, Journal of Intelligent Material Systems and Structures 28 (9) (2017) 1188–1210. doi:10.1177/1045389X16667552.

[22] W. C. Xing, Y. Q. Wang, Dynamic modeling and vibration analysis of bolted flange joint disk-drum structures: Theory and experiment, International Journal of Mechanical Sciences 272 (2024) 109186. doi:https://doi.org/10.1016/j.ijmecsci.2024.109186.

[23] S. Ren, H. Chen, R. Zheng, Modified time domain randomization technique for multi-shaker non-stationary non-gaussian random vibration control, Mechanical Systems and Signal Processing 213 (2024) 111311. doi:https://doi.org/10.1016/j.ymssp.2024.111311.

[24] R. Zheng, W. Xie, X. Wei, H. Chen, Limit strategy for multi-input multi-output random vibration control, Mechanical Systems and Signal Processing 195 (2023) 110293. doi:https://doi.org/10.1016/j.ymssp.2023.110293.

[25] W. Lei, Y. Jiang, X. Zeng, Z. Fan, A novel excitation signal generation technology for accelerated random vibration fatigue testing based on the law of kurtosis transmission, International Journal of Fatigue 159 (2022) 106835. doi:https://doi.org/10.1016/j.ijfatigue.2022.106835.

[26] H. Lu, J. Wang, Y. Lian, Z. Wen, T. Liu, Z. Yue, Effect of orientation deviation on random vibration fatigue behavior of nickel based single crystal superalloy, International Journal of Fatigue 177 (2023) 107930. doi:https://doi.org/10.1016/j.ijfatigue.2023.107930.

[27] B. Ellyson, M. Brochu, M. Brochu, Characterization of bending vibration fatigue of SLM fabricated Ti-6Al-4V, International Journal of Fatigue 99 (2017) 25–34. doi:https://doi.org/10.1016/j.ijfatigue.2017.02.005.

[28] M. Česnik, J. Slavič, M. Boltežar, Accelerated vibration-fatigue characterization for 3D-printed structures: Application to fused-filament-fabricated PLA samples, International Journal of Fatigue 171 (2023) 107574. doi:https://doi.org/10.1016/j.ijfatigue.2023.107574.

[29] H.-W.-X. Li, G. Lyngdoh, S. Doner, R. Yuan, D. Chelidze, Experimental monitoring and modeling of fatigue damage for 3D-printed polymeric beams under irregular loading, International Journal of Mechanical Sciences 233 (2022) 107626. doi:https://doi.org/10.1016/j.ijmecsci.2022.107626.

[30] M. Česnik, J. Slavič, Frequency-dependent fatigue properties of additively manufactured PLA, Polymers 16 (15) (2024). doi:doi.org/10.3390/polym16152147.

[31] A. Zorman, J. Slavič, M. Boltežar, Vibration fatigue by spectral methods – A review with open-source support, Mechanical Systems and Signal Processing 190 (2023) 110149. doi:https://doi.org/10.1016/j.ymssp.2023.110149.

[32] L. Shi, L. Khalij, C. Gautrelet, C. Shi, D. Benasciutti, Two-phase optimized experimental design for fatigue limit testing, Probabilistic Engineering Mechanics 75 (2024) 103551. doi:https://doi.org/10.1016/j.probengmech.2023.103551.

[33] H. Guan, H. Ma, X. Qu, Z. Wu, J. Zeng, Q. Xiong, H. Wang, Dynamic stress analysis of cracked rectangular blade: Simulation and ex-

periment, International Journal of Mechanical Sciences 267 (2024) 109015. doi:https://doi.org/10.1016/j.ijmecsci.2024.109015.

[34] C. Zhang, A. A. Mousavi, S. F. Masri, G. Gholipour, K. Yan, X. Li, Vibration feature extraction using signal processing techniques for structural health monitoring: A review, Mechanical Systems and Signal Processing 177 (2022) 109175. doi:https://doi.org/10.1016/j.ymssp.2022.109175.

[35] A. Staffa, M. Palmieri, G. Morettini, G. Zucca, F. Crocetti, F. Cianetti, Development and validation of a low-cost device for real-time detection of fatigue damage of structures subjected to vibrations, Sensors 23 (11) (2023). doi:10.3390/s23115143.

[36] M. A. Mousa, M. M. Yussof, T. S. Hussein, L. N. Assi, S. Ghahari, A digital image correlation technique for laboratory structural tests and applications: A systematic literature review, Sensors 23 (23) (2023). doi:https://www.mdpi.com/1424-8220/23/23/9362.

[37] Z. Qu, P. Jiang, W. Zhang, Development and application of infrared thermography non-destructive testing techniques, Sensors 20 (14) (2020). doi:https://www.mdpi.com/1424-8220/20/14/3851.

[38] J. Thalapil, S. Maiti, Detection of longitudinal cracks in long and short beams using changes in natural frequencies, International Journal of Mechanical Sciences 83 (2014) 38–47. doi:https://doi.org/10.1016/j.ijmecsci.2014.03.022.

[39] R. Janeliukstis, S. Ručevskis, S. Kaewunruen, Mode shape curvature squares method for crack detection in railway prestressed concrete sleepers, Engineering Failure Analysis 105 (2019) 386–401. doi:https://doi.org/10.1016/j.engfailanal.2019.07.020.

[40] S. K. Gupta, S. Das, Damage detection in a cantilever beam using noisy mode shapes with an application of artificial neural network-based improved mode shape curvature technique, Asian Journal of Civil Engineering 22 (2021) 1671–1693. doi:https://doi.org/10.1007/s42107-021-00404-w.

[41] Y. Zhang, Y. Luo, X. Guo, Y. Li, A new damage detection method of single-layer latticed shells based on combined modal strain energy index, Mechanical Systems and Signal Processing 172 (2022) 109011. doi:https://doi.org/10.1016/j.ymssp.2022.109011.

[42] Q. Bao, S. Yuan, F. Guo, A new synthesis aperture-MUSIC algorithm for damage diagnosis on complex aircraft structures, Mechanical Systems and Signal Processing 136 (2020) 106491. doi:https://doi.org/10.1016/j.ymssp.2019.106491.

[43] M. Risbet, P. Feissel, T. Roland, D. Brancherie, J.-M. Roelandt, Digital image correlation technique: Application to early fatigue damage detection in stainless steel, Procedia Engineering 2 (1) (2010) 2219–2227, Fatigue 2010. doi:https://doi.org/10.1016/j.proeng.2010.03.238.

[44] O. Kovářík, P. Haušild, J. Čapek, J. Medřický, J. Siegl, R. Mušálek, Z. Pala, N. Curry, S. Björklund, Resonance bending fatigue testing with simultaneous damping measurement and its application on layered coatings, International Journal of Fatigue 82 (2016) 300–309. doi:https://doi.org/10.1016/j.ijfatigue.2015.07.026.

[45] G. Sun, Y. Wang, Q. Luo, Q. Li, Vibration-based damage identification in composite plates using 3D-DIC and wavelet analysis, Mechanical Systems and Signal Processing 173 (2022) 108890. doi:https://doi.org/10.1016/j.ymssp.2022.108890.

[46] A. Zanarini, Mapping the defect acceptance for dynamically loaded components by exploiting DIC-based full-field receptances, Engineering Failure Analysis 163 (2024) 108385. doi:https://doi.org/10.1016/j.engfailanal.2024.108385.

[47] K. Zaletelj, J. Slavič, J. Šonc, M. Boltežar, Strain experimental modal analysis of an Euler–Bernoulli beam based on the thermoelastic principle, Mechanical Systems and Signal Processing 201 (2023) 110655. doi:https://doi.org/10.1016/j.ymssp.2023.110655.

[48] DIN EN 17119: Non-destructive testing - Thermographic testing - Active thermography (October 2018).

[49] E. D'Accardi, R. De Finis, G. Dell'Avvocato, G. Masciopinto, D. Palumbo, U. Galietti, Conduction thermography for non-destructive assessment of fatigue cracks in metallic materials, Infrared Physics & Technology 140 (2024) 105394. doi:https://doi.org/10.1016/j.infrared.2024.105394.

[50] W. Zhu, Z. Moumni, J. Zhu, Y. Zhang, Y. You, W. Zhang, A multiscale experimental investigation on fatigue crack propagation rate behavior of powder bed fusion-laser beam 316l stainless steel subjected to various heat treatments, Engineering Fracture Mechanics 302 (2024) 110064. doi:https://doi.org/10.1016/j.engfracmech.2024.110064.

[51] L. Bercelli, B. Levieil, C. Doudard, B. Malek, F. Bridier, A. Ezanno, Use of infrared thermography to model the effective stress ratio effect on fatigue crack growth in welded t-joints, Engineering Fracture Mechanics 279 (2023) 109061. doi:https://doi.org/10.1016/j.engfracmech.2023.109061.

[52] L. Bercelli, B. Levieil, C. Doudard, S. Calloch, Fatigue crack closure assessment by wavelet transform of infrared thermography signals, International Journal of Fatigue 190 (2025) 108639. doi:https://doi.org/10.1016/j.ijfatigue.2024.108639.

[53] M. Ricotta, G. Meneghetti, Estimating the intrinsic dissipation using the second-harmonic temperature signal in the tension–tension fatigue, Fatigue & Fracture of Engineering Materials & Structures 46 (11) (2023) 4218–4238. doi:https://doi.org/10.1111/ffe.14132.

[54] K. Amjad, P. Lambert, C. A. Middleton, R. J. Greene, E. A. Patterson, A thermal emissions-based real-time monitoring system for in situ detection of fatigue cracks, Proceedings of the Royal Society A: Mathematical, Physical and Engineering Sciences 478 (2266) (2022) 20210796. doi:10.1098/rspa.2021.0796.

[55] C. A. Middleton, K. Amjad, R. J. Greene, E. Hack, L. Harris, A. Kupferschmid, P. R. Lambert, E. A. Patterson, Industrial application of a low-cost structural health monitoring system in large-scale airframe tests, The Journal of Strain Analysis for Engineering Design 59 (3) (2024) 218–225. doi:10.1177/03093247231222951.

[56] R. De Finis, D. Palumbo, F. D. Carolo, M. Ricotta, G. Meneghetti, U. Galietti, Crack tip position evaluation and Paris' law assessment of a propagating crack by means of temperature-based approaches, Procedia Structural Integrity 39 (2022) 528–545, 7th International Conference on Crack Paths (CP2021). doi:https://doi.org/10.1016/j.prostr.2022.03.126.

[57] A. Quinlan, O. Castro, J. Dulieu-Barton, Towards assessment of fatigue damage in composite laminates using thermoelastic stress analysis, Composites Part C: Open Access 12 (2023) 100377. doi:https://doi.org/10.1016/j.jcomc.2023.100377.

[58] W. Christian, P. Lambert, I. Tabrizi, C. Middleton, C. Przybyla, E. Patterson, Towards automated characterisation of fatigue damage in composites using thermoelastic stress analysis, Composites Part A: Applied Science

and Manufacturing 183 (2024) 108205. doi:https://doi.org/10.1016/j.compositesa.2024.108205.

[59] F. de Sá Rodrigues, R. Marques, I. E. Tabrizi, A. Kefal, H. Q. Ali, M. Yildiz, A. Suleman, A new methodology for thermoelastic model identification in composite materials using digital image correlation, Optics and Lasers in Engineering 146 (2021) 106689. doi:https://doi.org/10.1016/j.optlaseng.2021.106689.

[60] L. Zheng, S. Wen, G. Yi, F. Li, Vibrations and thermoelastic quality factors of hemispherical shells with fillets, Thin-Walled Structures 201 (2024) 111996. doi:https://doi.org/10.1016/j.tws.2024.111996.

[61] Y. Tai, N. Chen, Thermoelastic damping in the out-of-plane vibration of a microring resonator with rectangular cross-section, International Journal of Mechanical Sciences 151 (2019) 684–691. doi:https://doi.org/10.1016/j.ijmecsci.2018.12.026.

[62] H. Zhou, X. Song, P. Li, Generalized thermoelastic dissipation in micro/nano-beams with two-dimensional heat conduction, International Journal of Mechanical Sciences 252 (2023) 108371. doi:https://doi.org/10.1016/j.ijmecsci.2023.108371.

[63] G. Tribbiani, T. Zara, T. Truffarelli, L. Capponi, Fiducial marker and blob detection-based motion compensation algorithm for Thermoelastic Stress Analysis measurements, Journal of Physics: Conference Series 2698 (1) (2024) 012001. doi:10.1088/1742-6596/2698/1/012001.

[64] Q. Wei, M. Han, J. Zhu, L. Zhuo, J. Huang, W. Li, W. Xie, Experimental and numerical investigation on detection fatigue crack in metallic plate by vibro-thermography, Infrared Physics & Technology 126 (2022) 104347. doi:https://doi.org/10.1016/j.infrared.2022.104347.

[65] H. Cai, J. Chen, G. Kou, Z. Zhao, Q. Xu, M. Liu, Y. Zhang, Z. Yang, Research on vibration fatigue behavior of blade structures based on infrared thermography, Infrared Physics & Technology 139 (2024) 105277. doi:https://doi.org/10.1016/j.infrared.2024.105277.

[66] L. Capponi, J. Slavič, G. Rossi, M. Boltežar, Thermoelasticity-based modal damage identification, International Journal of Fatigue 137 (2020) 105661. doi:https://doi.org/10.1016/j.ijfatigue.2020.105661.

[67] J. Šonc, K. Zaletelj, J. Slavič, Application of thermoelasticity in the frequency-domain multiaxial vibration-fatigue criterion, Mechanical Systems and Signal Processing 224 (2025) 112002. doi:https://doi.org/10.1016/j.ymssp.2024.112002.

[68] M. Česnik, J. Slavič, P. Čermelj, M. Boltežar, Frequency-based structural modification for the case of base excitation, Journal of Sound and Vibration 332 (20) (2013) 5029–5039. doi:doi.org/10.1016/j.jsv.2013.04.038.

[69] N. M. M. Maia, J. M. M. Silva, Theoretical and Experimental Modal Analysis, Research Studies Press Ltd., Baldock, Hertfordshire, 1997.

[70] H. Seon Park, J. Kim, B. K. Oh, Model updating method for damage detection of building structures under ambient excitation using modal participation ratio, Measurement 133 (2019) 251–261. doi:https://doi.org/10.1016/j.measurement.2018.10.023.

[71] T. Kranjc, J. Slavič, M. Boltežar, The mass normalization of the displacement and strain mode shapes in a strain experimental modal analysis using the mass-change strategy, Journal of Sound and Vibration 332 (26) (2013) 6968–6981. doi:https://doi.org/10.1016/j.jsv.2013.08.015.

[72] F. Li, H. Wu, P. Wu, Vibration fatigue dynamic stress simulation under

non-stationary state, Mechanical Systems and Signal Processing 146 (2021) 107006. doi:https://doi.org/10.1016/j.ymssp.2020.107006.

[73] J. S. Bendat, A. G. Piersol, Random Data: Analysis and Measurement Procedures, 4th Edition, Wiley, 2010.

[74] A. Wöhler, Versuche über die Festigkeit der Eisenbahnwagen-Achsen, Zeitschrift für Bauwesen 20 (1870) 73–106.

[75] A. Wong, R. Jones, J. Sparrow, Thermoelastic constant or thermoelastic parameter?, Journal of Physics and Chemistry of Solids 48 (8) (1987) 749–753. doi:https://doi.org/10.1016/0022-3697(87)90071-0.

[76] R. T. Potter, L. J. Greaves, The application of thermoelastic stress analysis techniques to fibre composites, in: D. Vukobratovich (Ed.), Optomechanical Systems Engineering, Vol. 0817, International Society for Optics and Photonics, SPIE, 1987, pp. 134 – 146. doi:10.1117/12.967419.

[77] W. N. Sharpe, Springer Handbook of Experimental Solid Mechanics, Springer Science & Business Media, 2008.

[78] C. J. W., T. J. W., An algorithm for the machine calculation of complex Fourier series, Mathematics of Computation 19 (90) (1965) 297–301.

[79] A. Kaľavský, A. Niesłony, R. Huňady, Influence of PSD estimation parameters on fatigue life prediction in spectral method, Materials 16 (3) (2023). doi:10.3390/ma16031007.

[80] B. Cauberghe, Applied frequency-domain system identification in the field of experimental and operational modal analysis, Ph.D. thesis, Vrije Universiteit Brussel (2004).